Nano Research

Open Access

Research Article

Surface engineering enabled highly sensitive humidity sensors in two-dimensional hexagonal boron nitride nanosheets

Wuyou Zhang[1,§], Jinxu Qin[1,§], Shoulong Lai[1], Hang Liu[1], Xigui Yang[1,2], and Chongxin Shan[1]

[1] Henan Key Laboratory of Diamond Optoelectronic Material and Devices, Key Laboratory of Integrated Circuit, Ministry of Education, School of Physics, Zhengzhou University, Zhengzhou 450052, China
[2] Institute of Quantum Materials and Physics, Henan Academy of Sciences, Zhengzhou 450046, China
[§] Wuyou Zhang and Jinxu Qin contributed equally to this work.

Cite this article: *Nano Research*, **2025**, *18*, 94907405. https://doi.org/10.26599/NR.2025.94907405

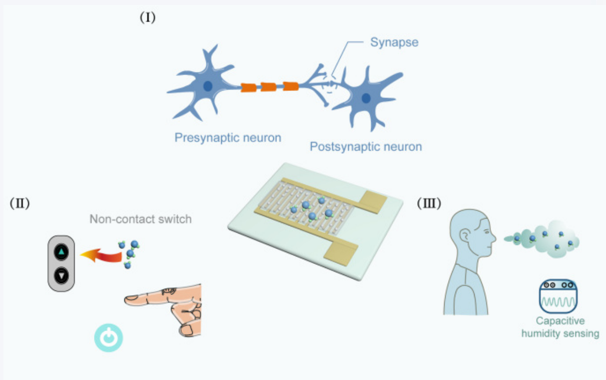

ABSTRACT: Humidity sensors have attracted considerable attention for their capability for real-time, continuous monitoring of critical physiological information, thus offering valuable insights into human health. Two-dimensional hexagonal boron nitride (h-BN) has emerged as an attractive material for humidity sensing due to its high specific surface area and excellent chemical stability. However, the low hydrophilicity of h-BN limits its ability to adsorb water molecules, resulting in reduced sensitivity and slow response times. Herein, capacitive humidity sensors consisted of amine-functionalized h-BN nanosheets have been developed. The introduction of amine groups modulates the hydrophilicity of pristine h-BN by forming hydrogen bonds, promoting interactions with water molecules. The h-BN-based sensor shows significantly improved performance, including high sensitivity (124,136 pF/%RH), large response (5,268,192%), and rapid response and recovery time (2.39 s/1.77 s). These findings demonstrate that amine functionalization can effectively enhance both water adsorption capacity and sensor performance, providing a promising approach for highly sensitive and responsive humidity sensors.

KEYWORDS: hexagonal boron nitride (h-BN), humidity sensor, high sensitivity, fast response, hydrogen bonding

1 Introduction

Humidity monitoring is crucial in a wide range of applications, from non-contact switches that detect environmental humidity changes to wearable devices in healthcare that assist professionals in making timely health assessments [1, 2]. Capacitive humidity sensors are favored for their stability, low power consumption, and simple structure [3]. However, challenges remain in realizing high sensitivity and fast response time [4]. Low sensitivity fails to detect subtle humidity variations, leading to inaccurate measurements, while slow response times hinder the sensor's ability to react to rapid fluctuations in dynamic environments [5].

Recent research has focused on improving capacitive humidity sensors through material engineering, particularly by incorporating two-dimensional (2D) materials [6]. These materials are attractive for humidity sensors due to their high surface area and tunable surface chemistry, which facilitates interaction and adsorption of water molecules [7, 8]. Furthermore, the surface properties of 2D materials can be tuned to enhance their affinity for water molecules [9]. Among the various two-dimensional materials, SnS_2 [10], black phosphorus [11], and borophene [12–16] have attracted significant attention due to their promising properties for various applications. However, challenges related to their stability and long-term reliability still need to be addressed for their practical deployment. Hexagonal boron nitride (h-BN) stands out for its exceptional chemical stability and reliability across a wide temperature range, making it an attractive candidate for high-performance capacitive humidity sensors [17]. However, despite these advantages, the interaction between h-BN and water molecules remains insufficient to fully exploit its potential in humidity sensing, thus necessitating further modifications to enhance its surface properties.

In this work, we developed high-performance capacitive humidity sensors based on amine-functionalized h-BN (A-h-BN)

Received: January 22, 2025; **Revised:** March 15, 2025
Accepted: March 26, 2025

Address correspondence to Xigui Yang, yangxg@zzu.edu.cn; Chongxin Shan, cxshan@zzu.edu.cn

and demonstrated their potential application in contactless sensing. The A-h-BN-based sensors exhibit high performance including quick response time of 2.39 s and fast recovery time of 1.77 s in a relative humidity (RH) range from 11% to 98%. Notably, the sensor achieves a sensitivity of 124,136 pF/%RH and a response of 5,268,192% at 98% RH with excellent repeatability and stability. The enhancement can be attributed to the high specific surface area of A-h-BN, which provides more active sites for water molecules, coupled with its increased hydrophilicity due to amine functionalization. Furthermore, the sensors exhibit synaptic-like behavior, where the capacitance increases with prolonged humidity pulse duration, and the recovery time extends, analogous to the learning and forgetting processes of brain. The sensors also demonstrate promising applications in distance detection and respiratory monitoring, accurately distinguishing between various distances and identifying different breathing patterns, etc.

2 Experimental

2.1 Amination treatment of h-BN

To prepare A-h-BN, 1 g h-BN purchased from Macklin Reagent was treated with ammonia solution. The h-BN was added to a beaker containing ammonia 30 mL of ammonia solution and stirred continuously using a magnetic stirrer at room temperature for 1 h, ensuring thorough interaction between the h-BN and ammonia. The mixture was then heated on a hot plate at 110 °C for 8 h to obtain the A-h-BN powder.

2.2 Materials characterization

The morphology of h-BN and A-h-BN was characterized using transmission electron microscope (TEM, Tecnai G20). The phase structures of both materials were analyzed by X-ray diffraction (XRD, D/MAX-3B) with Cu Kα radiation (λ = 1.5406 Å). Raman spectra were obtained using a Renishaw inVia Raman spectrometer, while Fourier-transform infrared (FT-IR) spectra were recorded in the range of 800–4000 cm^{-1} using a Thermo Scientific Nicolet iS 10 spectrometer. Additionally, XPS analysis was performed using an Escalab 250Xi spectrometer (Thermo Fisher Scientific) to further investigate the elemental composition and chemical bonding states.

2.3 Preparation of the A-h-BN-based capacitive humidity sensor

The A-h-BN powder was dispersed in deionized water to form a uniform suspension. Meanwhile, the polyethylene terephthalate (PET) substrate was cleaned multiple times with ethanol and deionized water to remove surface impurities. A mask template for the interdigital electrodes was placed on the cleaned PET substrate, and the electrodes were fabricated using magnetron sputtering. Each individual interdigital in the electrode has a length of 0.8 mm, a width of 0.1 mm, and a spacing of 0.1 mm. The electrode material used in the sensor is gold (Fig. S1 in the Electronic Supplementary Material (ESM)). After electrode fabrication, their structural integrity was inspected under a microscope. Indium particles were then used to connect the electrode terminals to wires. Using 15 mg of A-h-BN, we prepared an A-h-BN dispersion with a concentration of 0.151 mol/L by dissolving it in 4 mL of deionized water. We then evenly dropped 0.05 mL of the A-h-BN dispersion onto the interdigital electrodes and dried it, completing the fabrication of the capacitive humidity sensor [18].

2.4 Humidity sensing performance testing

At room temperature, the sensor's capacitance output at different RH levels was measured using a digital bridge (HIOKI IM3523 LCR HiTESTER). RH conditions were set using saturated salt solutions of LiCl, $MgCl_2$, K_2CO_3, NaBr, NaCl, KCl, and K_2SO_4, for RH levels of 11%, 32%, 43%, 57%, 75%, 84%, and 98%, respectively [19]. The definitions of sensitivity and response are as follows (Eqs. (1) and (2)) [20, 21]

$$S = \frac{C_X - C_0}{\mathrm{RH}_X - \mathrm{RH}_0} \tag{1}$$

$$R = \frac{C_X - C_0}{C_0} \tag{2}$$

Here, RH_X and RH_0 denote the RH levels of X% and 11%, respectively, while C_X and C_0 denote the sensor's capacitance output at X% RH and 11% RH, respectively.

2.5 First-principles calculations

First-principles calculations were performed using the Vienna *ab initio* simulation program package (VASP). The exchange-correlation energy was treated in the generalized gradient approximation using the Perdew–Burke–Ernzerhof functional. We calculated the adsorption energy of water molecules on h-BN and A-h-BN. One NH_2 radical has been constructed in the BN surface model to build the BN-NH_2 model, respectively. All models have been fully relaxed with the energy convergence criterion of 10^{-5} eV and the force convergence criterion of 0.02 eV/Å, respectively. The (2 × 2 × 1) K-points have been used in the K-point mesh. Additionally, we also computed the relative permittivity of A-h-BN as it adsorbs varying numbers of water molecules. The definition of adsorption energy (E_{ads}) and relative permittivity is provided as follows (Eqs. (3) and (4)) [22]

$$E_{\mathrm{ads}} = E_{\mathrm{total}} - E_{\mathrm{substrate}} - E_{\mathrm{adsorbate}} \tag{3}$$

$$C = \frac{\varepsilon A}{d} \tag{4}$$

where E_{total}, $E_{\mathrm{substrate}}$ and $E_{\mathrm{adsorbate}}$ represent the energy of adsorption structure, substrate and adsorbate, respectively. The C represents capacitance, ε represents relative permittivity, A represents plate area, and d represents plate distance.

3 Results and discussion

The h-BN features a high specific surface area and is easily modifiable, making it an ideal material for sensor applications [23]. The functionalization of h-BN includes amination [24], oxidation [25], fluorination [26–28], and others. High-temperature oxidation can damage the crystal structure of h-BN. Fluorination makes the surface more hydrophobic, which diminishes humidity response performance. In contrast, amination strengthens the material's adsorption of water molecules and significantly improves humidity response, offering distinct advantages. To enhance its hydrophilicity, the aminated treatment introduces amine groups on its surface, which are highly polar and can form hydrogen bonds with water molecules (Fig. 1(a)). The increased hydrophilicity of h-BN makes it easier to adsorb moisture, which is crucial for

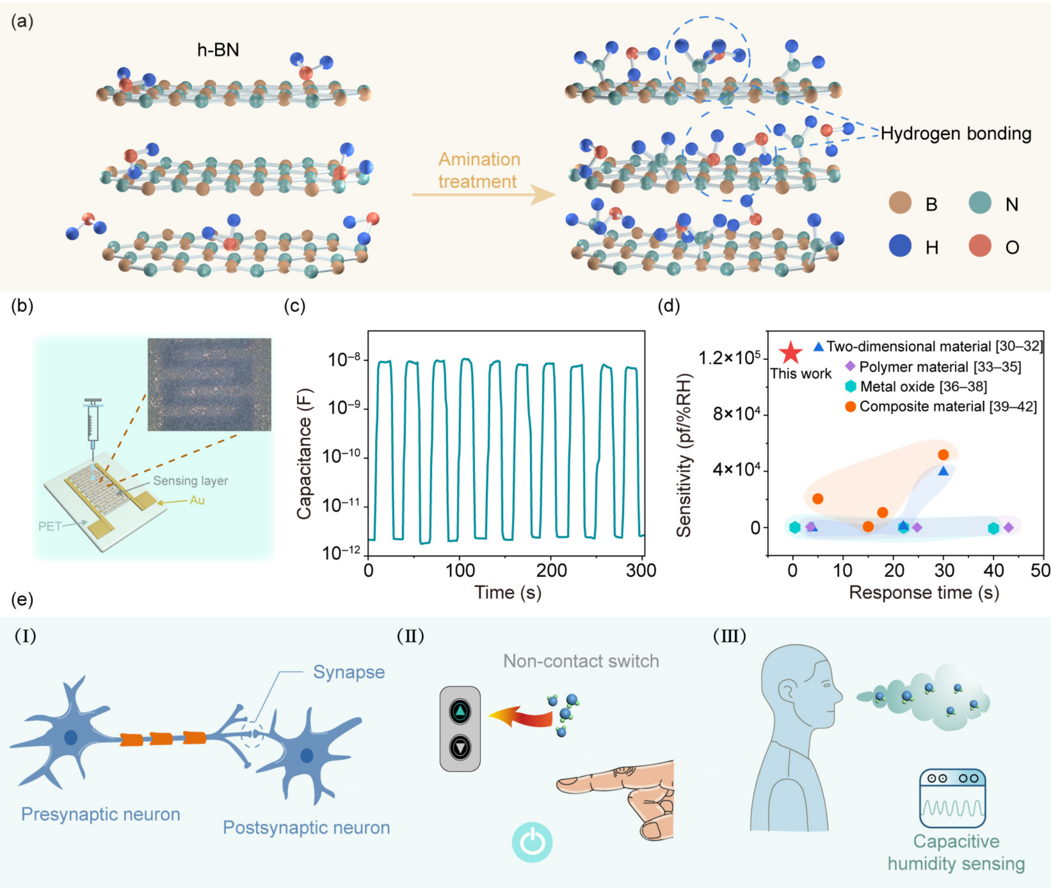

Figure 1 Hexagonal boron nitride nanosheets have good hygroscopic properties, and the sensors prepared from them show excellent performance. (a) Schematic illustration of water molecule adsorption on surface engineered h-BN. (b) Schematic illustration of the preparation process and a microscopic image of the sensor. (c) *C*–*t* curve of the sensor during the humidity cycle test. (d) Comparison of sensitivity and response time for reported capacitive humidity sensors. (e) Schematic illustration of the sensor applications, including (I) synaptic-like behavior, (II) non-contact human-machine interaction, and (III) respiratory monitoring.

humidity sensing. A-h-BN is dispersed in deionized water and then drop-cast onto interdigital electrodes to fabricate humidity sensors [29]. The microscopic image reveals that A-h-BN is uniformly distributed on the electrodes, ensuring consistent sensor performance (Fig. 1(b)). As shown in Fig. 1(c), the capacitance–time (*C*–*t*) curve of the sensor demonstrates reliable and repeatable behavior during the humidity cycle test, indicating excellent repeatability and stability of the sensor. When compared to other reported sensors, the A-h-BN-based sensor exhibits superior performance in terms of sensitivity and response time (Fig. 1(d)) [30–42]. This enhanced performance is attributed to the increased number of amine groups, which boosts its capacity to interact with water molecules and detect changes in humidity more effectively. The A-h-BN humidity sensor exhibits synaptic-like behavior, which is similar to the learning and forgetting processes of the human brain (Fig. 1(e)). Additionally, the sensor shows high repeatability and precision in detecting humidity variations at different distances, which could facilitate no-contact switch applications. In respiratory monitoring, the sensor's rapid response and stability enabling real-time detection of subtle humidity changes, which facilitating accurate identification of different breathing patterns. The versatility of A-h-BN sensors underscores their potential across diverse fields, including artificial intelligence-driven sensory technologies, human-machine interaction, and healthcare.

In this work, h-BN was treated in 25% ammonia solution for one hour, followed by drying on a heating plate to obtain ammonia modified h-BN. This amination treatment introduces additional amine groups to the surface, enhancing the ability to attract water molecules. Figures S2 and S3 in the ESM show TEM and high-resolution TEM (HRTEM) images, along with the corresponding fast Fourier transform (FFT) pattern for both h-BN and A-h-BN. The HRTEM image reveals a lattice spacing of 0.21 nm, corresponding to the (101) plane of h-BN [43]. The XRD patterns (Fig. 2(a)) of both the h-BN and A-h-BN show multiple peaks at 26.6°, 41.5°, 43.6°, 54.8°, 75.8°, and 82.0°, which align with the standard diffraction pattern of h-BN (JCPDS No. 34-0421) [44]. Raman spectra (Fig. 2(b)) show a characteristic peak at 1366 cm^{-1}, attributed to vibrations between boron and nitrogen atoms [45, 46]. These results indicate that the amination process does not disrupt the h-BN structure, and the B–N bond remains intact. As illustrated in Fig. 2(c), FT-IR spectra reveal two characteristic peaks at 800 and 1378 cm^{-1}, corresponding to B–N–B out-of-plane bending and B–N in-plane stretching modes, respectively [43]. A broad band around 3400 cm^{-1}, indicative of O–H stretching vibrations, is also observed [47]. After amination treatment, a new peak appears at 1650 cm^{-1}, corresponding to N–H bending vibrations [48]. The intensity of the 3400 cm^{-1} peak increases significantly, indicating a higher concentration of amine groups on the surface of A-h-BN [49, 50]. These results confirm that the amination treatment enhances the hydrophilicity of h-BN without compromising its

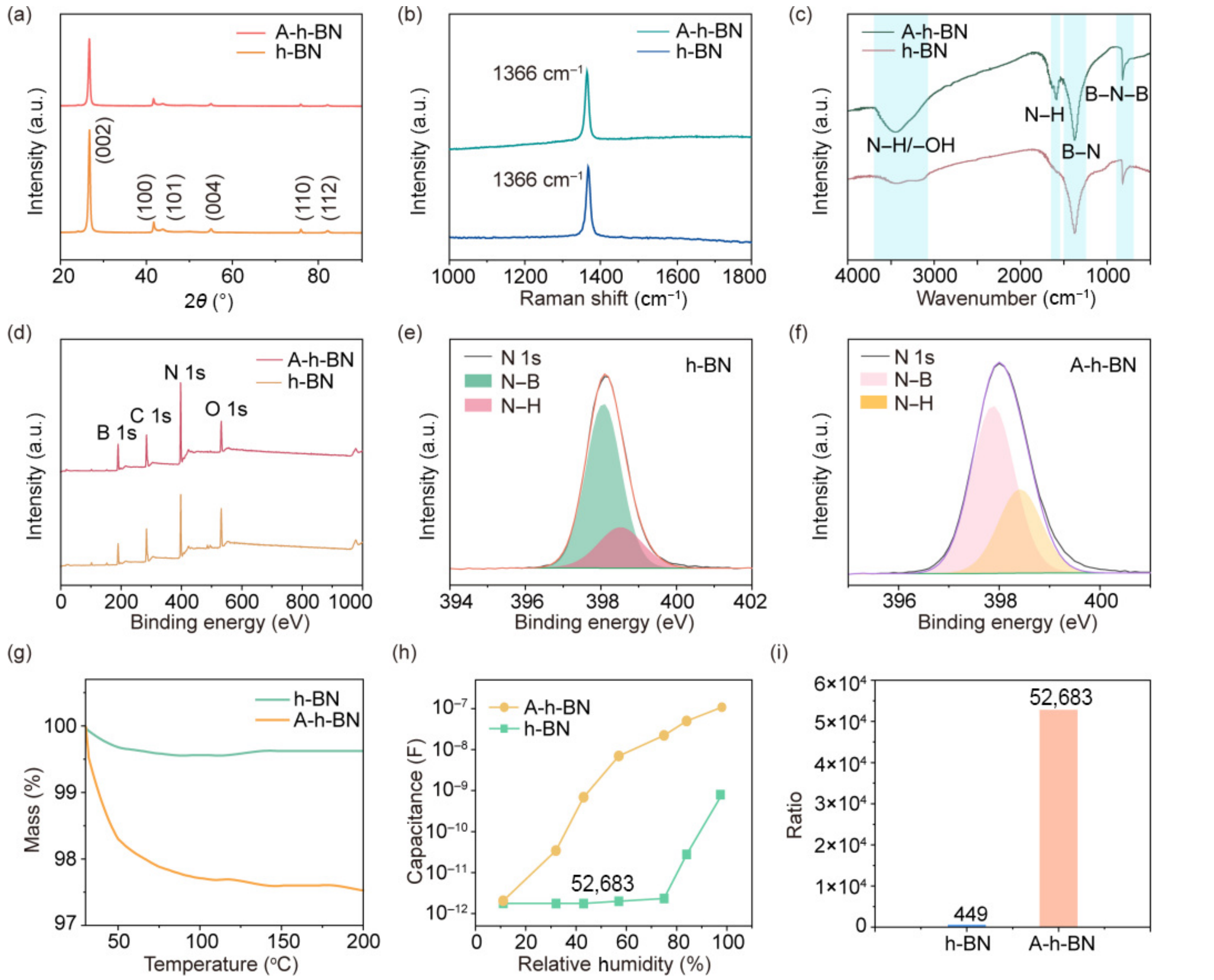

Figure 2 Characterization and performance comparison of h-BN nanosheets before and after amination treatment. (a) XRD patterns of the h-BN and A-h-BN. (b) Raman spectra of the h-BN and A-h-BN. (c) FT-IR spectra of the h-BN and A-h-BN. (d) Full XPS surveys spectra of the h-BN and A-h-BN. (e) High-resolution N 1s spectra of the h-BN. (f) High-resolution N 1s spectra of the A-h-BN. (g) TGA analysis of the h-BN and A-h-BN. (h) Comparison of the capacitance values for the h-BN and A-h-BN-based sensors at different RH levels. (i) Capacitive ratio of 98% RH to 11% RH for the h-BN and A-h-BN-based sensors.

structural integrity.

To further analyze the surface functional groups of the h-BN and A-h-BN, X-ray photoelectron spectroscopy (XPS) was performed. The full XPS spectra (Fig. 2(d)) show an increased nitrogen content in A-h-BN compared to h-BN. The presence of C and O elements is likely due to the adsorption of CO_2, H_2O, and O_2 on the surface [51]. High-resolution N 1s spectra (Figs. 2(e) and 2(f)) exhibit two distinct peaks corresponding to N–B and N–H bonds, with binding energies at 397.9 and 398.4 eV, respectively [52]. The increased intensity of the N–H peak confirms that the amine groups on the h-BN surface increases significantly after the treatment. Thermogravimetric analysis (TGA) in Fig. 2(g) illustrates that both the h-BN and A-h-BN lose weight below 100 °C due to the evaporation of surface water. However, A-h-BN exhibits a greater weight loss, indicating its enhanced hydrophilicity compared to untreated h-BN [53]. Dynamic vapor sorption (DVS) tests (Figs. S4 and S5 in the ESM) further confirm these findings: The h-BN shows negligible weight change at low RH levels, while the A-h-BN exhibits a significant increase in adsorption, particularly at high RH, indicating its improved ability to adsorb moisture. In terms of sensor performance, the h-BN-based sensor exhibits almost no change in capacitance output below 75% RH, whereas the A-h-BN sensor shows a clear increase in capacitance output with rising RH (Fig. 2(h)). Figure 2(i) presents the capacitance ratios of the sensors at 98% and 11% RH, with A-h-BN achieving a capacitance ratio of 52,683, significantly higher than the 449 observed for h-BN. These findings demonstrate the enhanced humidity response of the A-h-BN, suggesting that amination treatment improves the performance of the h-BN in capacitive humidity sensors significantly.

As the RH increases, more water molecules can be adsorbed on the surface of the A-h-BN (Fig. 3(a)), resulting in a change in capacitance output. Figure 3(b) shows the capacitance output at frequencies of 100 Hz, 1 kHz, 10 kHz, and 100 kHz, with RH varying from 11% to 98%. The data reveal that the sensor produces distinct capacitance values at different RH levels, with a gradual increase in capacitance as RH rises. Notably, capacitance decreases with increasing electric field frequencies, which is attributed to the delayed polarization of water molecules in response to the changing electric field [54]. At low frequencies, the electric field varies slowly, allowing water molecules sufficient time to complete the polarization process and effectively align with the field. This results in a higher relative permittivity and capacitance. In contrast, at high

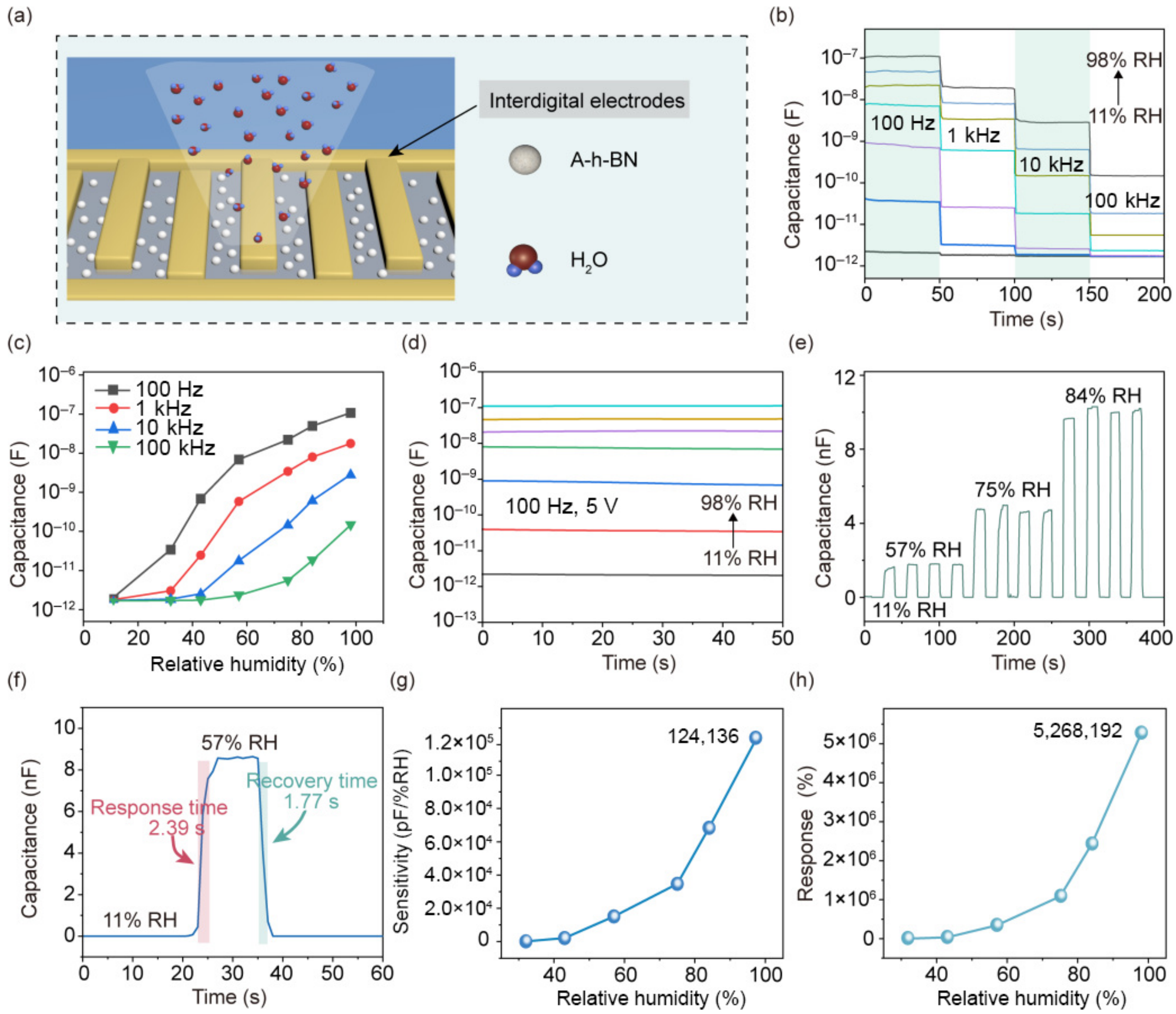

Figure 3 A-h-BN based humidity sensors performance test. (a) Schematic diagram illustrating the distribution of the A-h-BN on interdigital electrodes and its adsorption of water molecules. (b) *C*–*t* curves of the A-h-BN humidity sensor at different frequencies. (c) Capacitance output of the sensor under different frequencies and RH levels. (d) *C*–*t* curves of the humidity sensor under different levels of RH. (e) *C*–*t* curves of the A-h-BN humidity sensor from 11% RH to 84% RH. (f) The response and recovery curve of the A-h-BN humidity sensor. (g) Sensitivity of the A-h-BN sensor at different RH levels. (h) Response characteristics of the A-h-BN sensor at different RH levels.

frequencies, the polarization response of water molecules lags behind the rapidly oscillating electric field, preventing them from fully aligning. Consequently, the overall relative permittivity decreases, leading to a reduction in the sensor's capacitance output. Figure 3(c) shows the capacitance output as RH increases and the frequency decreases, revealing a clear relationship between capacitance and RH at different frequencies. The *C*–*t* curves at different RH levels demonstrate stable capacitance output, which indicates excellent stability and reliability for practical applications (Fig. 3(d)). The dynamic humidity response and recovery tests of the sensor demonstrate excellent repeatability when responding to varying RH levels (Fig. 3(e)). The sensor's response and recovery times are 2.39 and 1.77 s, respectively, demonstrating its rapid response to humidity changes (Fig. 3(f)). The sensor demonstrated outstanding consistency in response and recovery times during repeatability tests (Fig. S6 in the ESM). Figures 3(g) and 3(h) present the sensitivity and response of the A-h-BN-based sensor. At 98% RH, the sensor achieves a sensitivity of 124,136 pF/%RH and a response of 5,268,192%. These results demonstrate the excellent performance of the A-h-BN sensor in terms of RH response range, sensitivity, and response/recovery times, surpassing the performance of other humidity sensors, as summarized in Table 1.

Signal transmission between adjacent neurons occurs via biological synapses, where neurotransmitter release at the presynaptic membrane influences the postsynaptic response [55]. Similarly, in a humidity sensor, humidity pulses act as presynaptic inputs, while the capacitance output serves as the postsynaptic response. Figure 4(a) illustrates how neurotransmitter release at the presynaptic membrane affects the postsynaptic response. Figure 4(b) shows the sensor's response to two consecutive humidity pulses, with the capacitance output during the second pulse being higher than that of the first, resembling paired-pulse facilitation (PPF) observed in neural synapses [56]. Further analysis reveals that increasing the width of the humidity pulses results in a higher capacitance output and a longer recovery time (Fig. 4(c)). This behavior is due to changes in the sensor's sensing layer, located above the interdigital electrodes, which alters its relative permittivity as water molecules are adsorbed. This change in capacitance

Table 1 Comparison of this work with previously reported capacitive humidity sensors

Sensing material	RH range	Sensitivity (pF/%RH)	Response/recovery time (s/s)	References
BP	15–90	10	3.9/1	[30]
GO/CNF	11–97	1146.8	22/2	[31]
GO	55–95	40,000	30/150	[32]
Cleancool fibers	6–97	82.4	3.5/4	[33]
cellulose nanofiber	11–95	27.95	43/1	[34]
PMDA/ODA	10–90	1.24	25/25	[35]
ITO	5–95	7.76	21.4/4.8	[36]
TiO_2	5–95	1.3	0.4/0.9	[37]
PVDF-$BaTiO_3$	40–90	0.2516	40/25	[38]
$CsPb_2Br_5$/ $BaTiO_3$	25–95	21,426.6	5/5	[39]
CNF/ GOQD	11–97	51,840.91	30/11	[40]
In_2O_3/GO	11–97	1061.6	15/2.5	[41]
SnS_2/Zn_2SnO_4	0–97	10,709	18/1	[42]
A-h-BN	11–98	124,136	2.39/1.77	This work

enables the sensor to detect even subtle variations in humidity levels with high precision (Fig. 4(d)). The sensor also exhibits strong performance in practical applications, such as non-contact switch and respiratory monitoring. Non-contact human-machine interaction eliminates the need for direct physical contact with devices, enhancing convenience and hygiene, especially in environments where touchless operation is required (Fig. 4(e)) [57–60]. The capacitance increases as the finger approaches, and decreases as the finger moves away. This capability is ideal for non-contact switch mechanisms in smart devices. Figure 4(f) further quantifies the relationship between fingertip distance and capacitance output, showing distinct capacitance values at distances of 5, 10, and 15 mm, demonstrating the sensor's sensitivity to distance. In respiratory monitoring, the sensor's ability to detect subtle humidity changes is valuable for tracking breathing patterns and rates, aiding in the early detection of respiratory conditions [61–63]. Figure 4(g) illustrates the sensor's application in respiratory monitoring, where the sensor can accurately identify different breathing states—normal, fast, slow, and deep breaths, by measuring the output. This capability is essential for monitoring physiological conditions and ensuring timely detection of health

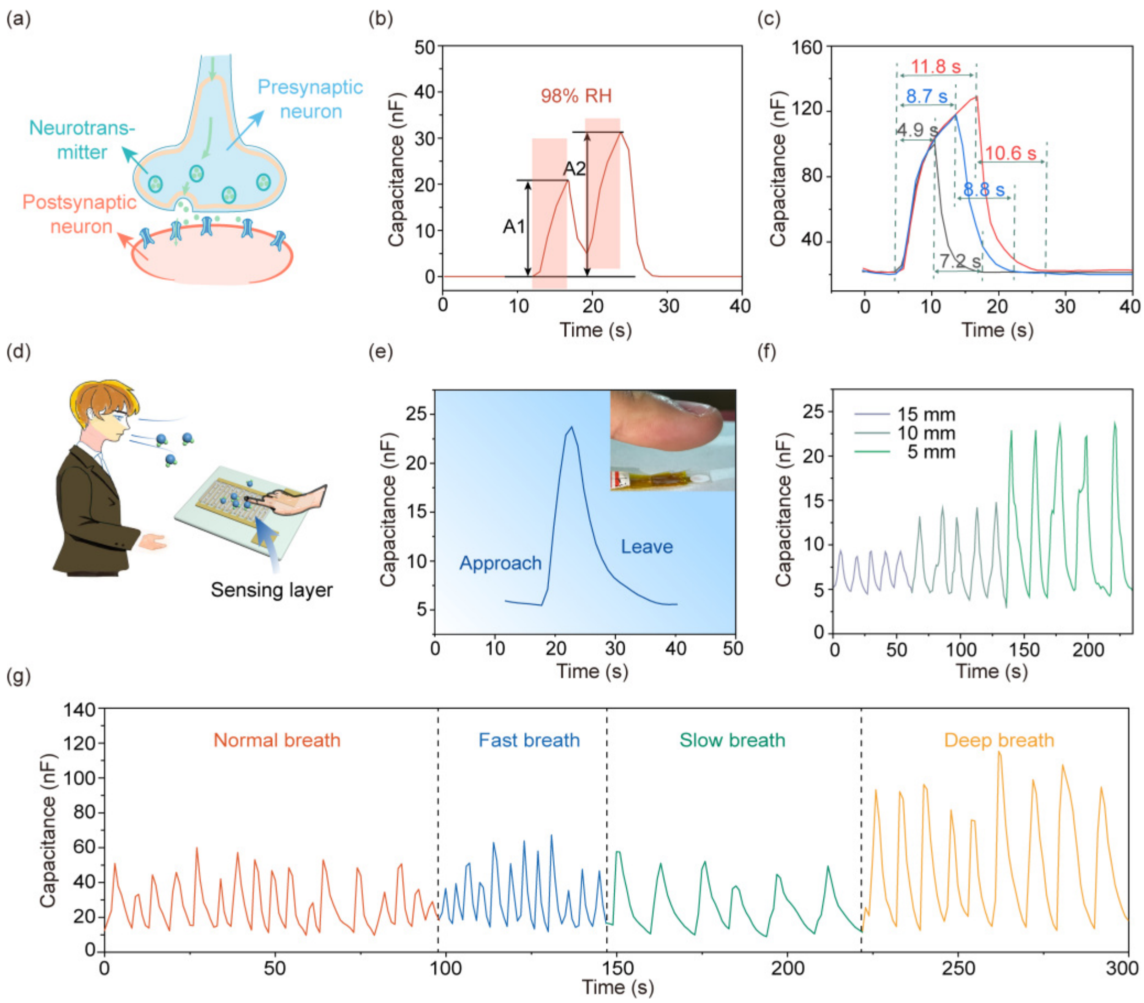

Figure 4 A-h-BN based humidity sensors show great advantages in practical applications. (a) Schematic illustration of a biological synapse. (b) *C–t* curve of the sensor under two consecutive humidity pulses. (c) Relationship between recovery time and capacitance output at different RH pulse widths. (d) Schematic illustration of the humidity sensor applied in non-contact human–machine interaction and respiratory monitoring. (e) Application of the humidity sensor as a non-contact switch, with the inset showing a finger approaching and moving away from the sensor. (f) *C–t* curve of the humidity sensor at varying fingertip distances. (g) *C–t* curve of the humidity sensor for different breathing patterns (normal, fast, slow, and deep breaths).

issues. The sensor's anti-interference ability in practical applications is further evaluated. By testing its capacitance output under different temperatures and gas environments, it is verified that the sensor has excellent anti-interference performance (Fig. S7 in the ESM).

To further explore the performance of the A-h-BN humidity sensor, we employed density functional theory (DFT) to calculate the adsorption energy of water molecules on both h-BN and A-h-BN [64, 65]. Figure 5(a) shows the adsorption process, illustrating how water molecules interact with the surface of both materials. The calculations reveal that the adsorption energy for a single water molecule is significantly stronger for A-h-BN (−0.354 eV) than for h-BN (−0.156 eV) (Fig. 5(b)). This indicates that A-h-BN has a higher affinity for water molecules, suggesting that the amine groups on A-h-BN enhance its hydrophilicity [66]. Figure 5(c) depicts the structural models of A-h-BN adsorbing different numbers of water molecules (0, 1, 2, and 3). We then calculated the relative permittivity (ε) for each model, yielding values of 1.28, 1.29, 1.31, and 1.32, respectively, for 0, 1, 2, and 3 water molecules (Fig. 5(d)). These results demonstrate that as the number of adsorbed water molecules increases, the relative permittivity of A-h-BN rises, leading to higher capacitance output. This increase in capacitance is attributed to the water molecules occupying the interstitial spaces within A-h-BN, replacing air. Given that water has a relative permittivity of 78, compared to air's value of 1, the adsorption of water significantly enhances the material's overall permittivity [67]. The highest capacitance output is observed when the sensor is exposed to air, but is lower in oxygen, nitrogen, vacuum, indicating that water molecules in the air are the primary factor driving the sensor's output variations (Fig. 5(e)). This result further reinforces that the sensor's performance is strongly dependent on the presence of water molecules and not influenced by other gases like oxygen or nitrogen.

As the RH rises, the amine groups on the surface of A-h-BN adsorb water molecules forming hydrogen bonds that enhance water molecules adsorption (Fig. 5(f)) [68]. Moreover, intermolecular hydrogen bonding can occur between the oxygen atom of one water molecule and the hydrogen atoms of adjacent water molecules [69]. This network of hydrogen bonds enhances the overall adsorption capacity and facilitates the aggregation of water molecules on the A-h-BN surface. The extensive hydrogen bond network significantly enhances the adsorption capacity of the A-h-BN for water molecules, thereby improving the performance of the A-h-BN-based humidity sensors.

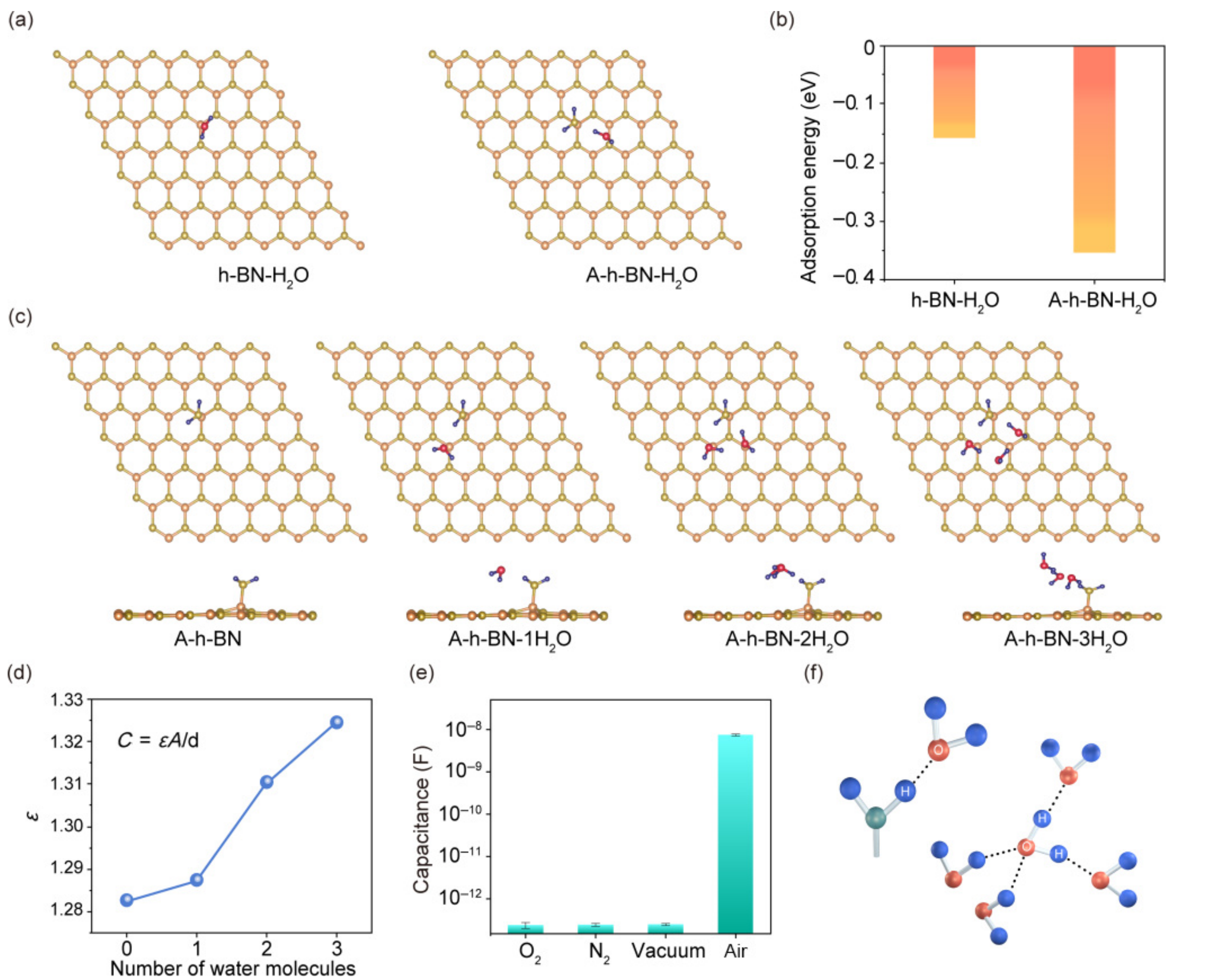

Figure 5 Analyze the sensing mechanism through theoretical calculation. (a) Schematic of h-BN and A-h-BN adsorbing a single water molecule. (b) Adsorption energy of water molecule on h-BN and A-h-BN. (c) Model schematic of A-h-BN adsorbing different numbers of water molecules (0, 1, 2, and 3). (d) Relationship between the relative permittivity and the number of water molecules. (e) Capacitance output of the A-h-BN humidity sensor under oxygen, nitrogen, vacuum and air atmospheres. (f) Schematic illustration of hydrogen bonding formed when A-h-BN adsorbs water.

4 Conclusions

In summary, we present a surface engineering strategy to enhance the performance of humidity sensors based on 2D h-BN nanosheets through amination treatment. The optimized sensors show impressive improvements over conventional designs, including a broad humidity detection range (11%–98% RH), high sensitivity (124,136 pF/%RH) and response (5,268,192%), as well as rapid response (2.39 s) and recovery times (1.77 s). Theoretical calculations reveal that hydrogen bonding between water molecules and amine groups on A-h-BN contributes to the enhanced water adsorption capacity and overall sensor performance. With its high sensing performance, the A-h-BN sensors demonstrate advanced capabilities, such as synaptic-like behavior, distance detection, and respiratory monitoring. These findings underscore how functionalizing h-BN can significantly improve its ability to humidity changes. By exploiting the hydrophilicity and hydrogen bonding interactions, the A-h-BN based sensors achieve both high sensitivity and stable performance. As a result, h-BN holds great promise for applications requiring precise humidity monitoring, including non-contact human-machine interaction, environmental sensing, and healthcare devices.

Electronic Supplementary Material: Supplementary material (interdigital electrode structure, TEM images, DVS tests, response time repeatability test, and anti-interference test) is available in the online version of this article at https://doi.org/10.26599/NR.2025.94907405.

Data availability

All data needed to support the conclusions in the paper are presented in the manuscript and the ESM. Additional data related to this paper may be requested from the corresponding author upon request.

Acknowledgements

This work was supported by the National Key Research and Development Program of China (No. 2024YFE0105200), and the National Natural Science Foundation of China (Nos. 62422408, 12374016, 12174348, and 62027816).

Declaration of competing interest

The authors declare no conflict of interests.

Author contribution statement

W. Y. Z.: Data curation, investigation, writing – original draft. J. X. Q.: Data curation, investigation, resources. S. L. L.: Data curation, formal analysis, investigation. H. L.: Data curation, formal analysis, investigation. X. G. Y.: Conceptualization, funding acquisition, project administration, supervision, writing – review & editing. C. X. S.: Conceptualization, funding acquisition, project administration, supervision, writing – review & editing.

Use of AI statement

None.

References

[1] Ni, Q. C.; Lou, Q.; Shen, C. L.; Zheng, G. S.; Song, R. W.; Hao, J. N.; Liu, J. L.; Zhu, J. Y.; Zang, J. H.; Dong, L. et al. Sensitive humidity sensor based on moisture-driven energy generation. *Nano Res.* **2024**, *17*, 5578–5586.

[2] Zhou, J. K.; Li, J.; Jia, H. L.; Yao, K. M.; Jia, S. X.; Li, J. Y.; Zhao, G. Y.; Yiu, C. K.; Gao, Z.; Li, D. F. et al. Mormyroidea-inspired electronic skin for active non-contact three-dimensional tracking and sensing. *Nat. Commun.* **2024**, *15*, 9875.

[3] Qin, J.; Yin, L. J.; Hao, Y. N.; Zhong, S. L.; Zhang, D. L.; Bi, K.; Zhang, Y. X.; Zhao, Y.; Dang, Z. M. Flexible and stretchable capacitive sensors with different microstructures. *Adv. Mater.* **2021**, *33*, 2008267.

[4] Li, J. Q.; Fang, Z. P.; Wei, D. S.; Liu, Y. Flexible pressure, humidity, and temperature sensors for human health monitoring. *Adv. Healthc. Mater.* **2024**, *13*, 2401532.

[5] Pyo, S.; Lee, J.; Bae, K.; Sim, S.; Kim, J. Recent progress in flexible tactile sensors for human-interactive systems: From sensors to advanced applications. *Adv. Mater.* **2021**, *33*, 2005902.

[6] Ali, S.; Hassan, A.; Hassan, G.; Bae, J.; Lee, C. H. All-printed humidity sensor based on graphene/methyl-red composite with high sensitivity. *Carbon* **2016**, *105*, 23–32.

[7] Lei, D. D.; Zhang, Q. X.; Liu, N. S.; Su, T. Y.; Wang, L. X.; Ren, Z. Q.; Zhang, Z.; Su, J.; Gao, Y. H. Self-powered graphene oxide humidity sensor based on potentiometric humidity transduction mechanism. *Adv. Funct. Mater.* **2022**, *32*, 2107330.

[8] Torres Alonso, E.; Shin, D. W.; Rajan, G.; Neves, A. I. S.; Russo, S.; Craciun, M. F. Water-based solution processing and wafer-scale integration of all-graphene humidity sensors. *Adv. Sci.* **2019**, *6*, 1802318.

[9] Khosla, A.; Sonu; Awan, H. T. A.; Singh, K.; Gaurav; Walvekar, R.; Zhao, Z. H.; Kaushik, A.; Khalid, M.; Chaudhary, V. Emergence of MXene and MXene-polymer hybrid membranes as future-environmental remediation strategies. *Adv. Sci.* **2022**, *9*, 2203527.

[10] Liu, J.; Zhang, J. N.; Yu, Q.; Liu, Y. M.; Zhang, X. L.; Zhu, G. Q.; Jia, Y. M.; Lu, H. B.; Gao, J. Z.; Wang, H. J. et al. Flexible, breathable and hydrophobic SnO_2–SnS_2–SiO_2/SiO_2 all-inorganic self-supporting nanofiber membrane for ultralow-concentration NO_2 sensing under high humidity. *Adv. Funct. Mater.* **2025**, *35*, 2410833.

[11] Yasaei, P.; Behranginia, A.; Foroozan, T.; Asadi, M.; Kim, K.; Khalili-Araghi, F.; Salehi-Khojin, A. Stable and selective humidity sensing using stacked black phosphorus flakes. *ACS Nano* **2015**, *9*, 9898–9905.

[12] Hou, C.; Tai, G. A.; Hao, J. Q.; Sheng, L. H.; Liu, B.; Wu, Z. T. Ultrastable crystalline semiconducting hydrogenated borophene. *Angew. Chem., Int. Ed.* **2020**, *59*, 10819–10825.

[13] Hou, C.; Tai, G. A.; Wu, Z. H.; Hao, J. Q. Borophene: Current status, challenges and opportunities. *ChemPlusChem* **2020**, *85*, 2186–2196.

[14] Wu, Z. H.; Tai, G. A.; Liu, R. S.; Shao, W.; Hou, C.; Liang, X. C. Synthesis of borophene on quartz towards hydroelectric generators. *J. Mater. Chem. A* **2022**, *10*, 8218–8226.

[15] Liang, X. C.; Hou, C.; Wu, Z. H.; Wu, Z. T.; Tai, G. A. Multilayer α'-4H-borophene growth on gallium arsenide towards high-performance near-infrared photodetector. *Nanotechnology* **2023**, *34*, 205701.

[16] Liu, Y.; Tai, G. A.; Hou, C.; Wu, Z. T.; Liang, X. C. Chemical vapor deposition growth of few-layer β_{12}-borophane on copper foils toward broadband photodetection. *ACS Appl. Mater. Interfaces* **2023**, *15*, 14566–14574.

[17] Naclerio, A. E.; Kidambi, P. R. A review of scalable hexagonal boron nitride (*h*-BN) synthesis for present and future applications. *Adv. Mater.* **2023**, *35*, 2207374.

[18] Qin, J. X.; Yang, X. G.; Lv, C. F.; Li, Y. Z.; Chen, X. X.; Zhang, Z. F.; Zang, J. H.; Yang, X.; Liu, K. K.; Dong, L. et al. Humidity sensors realized via negative photoconductivity effect in nanodiamonds. *J. Phys. Chem. Lett.* **2021**, *12*, 4079–4084.

[19] Lv, S. J.; Shuai, L. Z.; Ding, W. F.; Ke, W. Q.; Wang, B.; Wan, J. M. Flexible humidity sensitive fiber with swellable metal-organic frameworks. *Adv. Fiber Mater.* **2021**, *3*, 107–116.
[20] Shen, Y. K.; Hou, S. J.; Hao, D. D.; Zhang, X.; Lu, Y.; Zu, G. Q.; Huang, J. Food-based highly sensitive capacitive humidity sensors by inkjet printing for human body monitoring. *ACS Appl. Electron. Mater.* **2021**, *3*, 4081–4090.
[21] Arman Kuzubasoglu, B. Recent studies on the humidity sensor: A mini review. *ACS Appl. Electron. Mater.* **2022**, *4*, 4797–4807.
[22] Kim, K.; Park, Y. G.; Hyun, B. G.; Choi, M.; Park, J. U. Recent advances in transparent electronics with stretchable forms. *Adv. Mater.* **2019**, *31*, 1804690.
[23] Yoo, S. C.; Park, Y. K.; Park, C.; Ryu, H.; Hong, S. H. Biomimetic artificial nacre: Boron nitride nanosheets/gelatin nanocomposites for biomedical applications. *Adv. Funct. Mater.* **2018**, *28*, 1805948.
[24] Hao, Y. J.; Liu, F.; Guo, X. Y.; Wang, H. Q.; Li, J.; Pan, J.; Huang, L. L. Super-hydrophilic polyetherimide membrane with surface amino exposed for highly efficient oil-water separation. *Fibers Polym.* **2024**, *25*, 817–828.
[25] Mazhar, H.; Adamson, D. H.; Al-Harthi, M. A. Differently oxidized portions of functionalized hexagonal boron nitride. *Mater. Chem. Phys.* **2023**, *308*, 128243.
[26] Peng, Z. H.; Song, J.; Gao, Y.; Liu, J.; Lee, C.; Chen, G. R.; Wang, Z. K.; Chen, J.; Leung, M. K. H. A fluorinated polymer sponge with superhydrophobicity for high-performance biomechanical energy harvesting. *Nano Energy* **2021**, *85*, 106021.
[27] Meiyazhagan, A.; Serles, P.; Salpekar, D.; Oliveira, E. F.; Alemany, L. B.; Fu, R. Q.; Gao, G. H.; Arif, T.; Vajtai, R.; Swaminathan, V. et al. Gas-phase fluorination of hexagonal boron nitride. *Adv. Mater.* **2021**, *33*, 2106084.
[28] Serre, C. Superhydrophobicity in highly fluorinated porous metal-organic frameworks. *Angew. Chem., Int. Ed.* **2012**, *51*, 6048–6050.
[29] Liu, Y.; Tian, Y. M.; Liu, F. M.; Gu, T. Y.; Wang, B.; He, J. M.; Wang, C.; Meng, X.; Sun, P.; Lu, G. Y. Multilayer fluorine-free MoBTx MBene with hydrophilic structural-modulating for the fabrication of a low-resistance and high-resolution humidity sensor. *Adv. Sci.* **2024**, *11*, 2404178.
[30] Chen, W. H.; Huang, J. Q.; Zhu, C. Y.; Xu, F.; Huang, Q. A. An interdigital capacitive humidity sensor with layered black phosphorus flakes as a sensing material. *IEEE Sens. J.* **2019**, *19*, 11007–11013.
[31] Li, X. Y.; Cai, F. K.; Cao, J. P.; Fu, N.; Dong, Z. C.; Long, N.; Zhao, J.; Yao, Y. F. Graphene oxide/cellulose nanofiber-based capacitive humidity sensor with high sensitivity. *Sens. Actuators A Phys.* **2024**, *368*, 115064.
[32] Vasiljević, D. Z.; Mansouri, A.; Anzi, L.; Sordan, R.; Stojanović, G. M. Performance analysis of flexible ink-jet printed humidity sensors based on graphene oxide. *IEEE Sens. J.* **2018**, *18*, 4378–4383.
[33] Ma, L. Y.; Wu, R. H.; Patil, A.; Zhu, S. H.; Meng, Z. H.; Meng, H. Q.; Hou, C.; Zhang, Y. F.; Liu, Q.; Yu, R. et al. Full - textile wireless flexible humidity sensor for human physiological monitoring. *Adv. Funct. Mater.* **2019**, *29*, 1904549.
[34] Hou, Z. N.; Ma, Z. Y.; Guan, X.; Zhao, H. R.; Liu, S.; Fei, T.; Zhang, T. A cellulose nanofiber capacitive humidity sensor with high sensitivity and fast recovery characteristics. *Chemosensors* **2022**, *10*, 464.
[35] Qiang, T.; Wang, C.; Liu, M. Q.; Adhikari, K. K.; Liang, J. G.; Wang, L.; Li, Y.; Wu, Y. M.; Yang, G. H.; Meng, F. Y. et al. High-performance porous MIM-type capacitive humidity sensor realized via inductive coupled plasma and reactive-Ion etching. *Sens. Actuators B Chem.* **2018**, *258*, 704–714.
[36] McGhee, J. R.; Sagu, J. S.; Southee, D. J.; Evans, P. S. A.; Wijayantha, K. G. U. Printed, fully metal oxide, capacitive humidity sensors using conductive indium tin oxide inks. *ACS Appl. Electron. Mater.* **2020**, *2*, 3593–3600.
[37] Mahaseth, D. N.; Islam, T. An ultrafast capacitive humidity sensor with excellent static and dynamic characteristics. *IEEE Sens. J.* **2024**, *24*, 8674–8681.
[38] Mallick, S.; Ahmad, Z.; Qadir, K. W.; Rehman, A.; Shakoor, R. A.; Touati, F.; Al-Muhtaseb, S. A. Effect of $BaTiO_3$ on the sensing properties of PVDF composite-based capacitive humidity sensors. *Ceram. Int.* **2020**, *46*, 2949–2953.
[39] Cho, M. Y.; Kim, S.; Kim, I. S.; Kim, E. S.; Wang, Z. J.; Kim, N. Y.; Kim, S. W.; Oh, J. M. Perovskite-induced ultrasensitive and highly stable humidity sensor systems prepared by aerosol deposition at room temperature. *Adv. Funct. Mater.* **2020**, *30*, 1907449.
[40] Huang, L. J.; Yang, Y. T.; Ti, P.; Su, G. T.; Yuan, Q. P. Graphene oxide quantum dots attached on wood-derived nanocellulose to fabricate a highly sensitive humidity sensor. *Carbohydr. Polym.* **2022**, *288*, 119312.
[41] Li, B. L.; Tian, Q.; Su, H. X.; Wang, X. W.; Wang, T. E.; Zhang, D. Z. High sensitivity portable capacitive humidity sensor based on In_2O_3 nanocubes-decorated GO nanosheets and its wearable application in respiration detection. *Sens. Actuators B Chem.* **2019**, *299*, 126973.
[42] Zhang, D. Z.; Zong, X. Q.; Wu, Z. L.; Zhang, Y. Hierarchical self-assembled SnS_2 nanoflower/Zn_2SnO_4 hollow sphere nanohybrid for humidity-sensing applications. *ACS Appl. Mater. Interfaces* **2018**, *10*, 32631–32639.
[43] Radhakrishnan, S.; Das, D.; Samanta, A.; De Los Reyes, C. A.; Deng, L. Z.; Alemany, L. B.; Weldeghiorghis, T. K.; Khabashesku, V. N.; Kochat, V.; Jin, Z. H. et al. Fluorinated h-BN as a magnetic semiconductor. *Sci. Adv.* **2017**, *3*, e1700842.
[44] He, M. K.; Zhong, X.; Lu, X. H.; Hu, J. W.; Ruan, K. P.; Guo, H.; Zhang, Y. L.; Guo, Y. Q.; Gu, J. W. Excellent low-frequency microwave absorption and high thermal conductivity in polydimethylsiloxane composites endowed by hydrangea-like CoNi@BN heterostructure fillers. *Adv. Mater.* **2024**, *36*, 2410186.
[45] Wang, G. K.; Huang, J. D.; Zhang, S. Y.; Meng, J. H.; Chen, J. R.; Shi, Y. M.; Jiang, J.; Li, J. Z.; Cheng, Y.; Zeng, L. B. et al. Wafer-scale single crystal hexagonal boron nitride layers grown by submicron-spacing vapor deposition. *Small* **2023**, *19*, 2301086.
[46] Huang, C. J.; Chen, C.; Zhang, M. W.; Lin, L. H.; Ye, X. X.; Lin, S.; Antonietti, M.; Wang, X. C. Carbon-doped BN nanosheets for metal-free photoredox catalysis. *Nat. Commun.* **2015**, *6*, 7698.
[47] Liu, H.; Qin, J. X.; Yang, X. G.; Lv, C. F.; Huang, W. T.; Li, F. K.; Zhang, C.; Wu, Y. R.; Dong, L.; Shan, C. X. Highly sensitive humidity sensors based on hexagonal boron nitride nanosheets for contactless sensing. *Nano Res.* **2023**, *16*, 10279–10286.
[48] Wu, X. F.; Zhao, Z. H.; Sun, Y.; Li, H.; Wang, Y. J.; Zhang, C. X.; Gong, X. D.; Wang, Y. D.; Yang, X. Y.; Liu, Y. Boron nitride nanoparticles with high specific surface area: Preparation by a calcination method and application in epoxy resin. *J. Inorg. Organomet. Polym. Mater.* **2017**, *27*, 1142–1147.
[49] Weng, Q. H.; Kvashnin, D. G.; Wang, X.; Cretu, O.; Yang, Y. J.; Zhou, M.; Zhang, C.; Tang, D. M.; Sorokin, P. B.; Bando, Y. et al. Tuning of the optical, electronic, and magnetic properties of boron nitride nanosheets with oxygen doping and functionalization. *Adv. Mater.* **2017**, *29*, 1700695.
[50] Takagaki, A.; Nakamura, S.; Ashimura, S.; Yoshida, M.; Song, J. T.; Watanabe, M.; Hayashi, S.; Ishihara, T. Mixing nitrogen-containing compounds for synthesis of porous boron nitride for improved porosity, surface functionality, and solid base catalytic activity. *Appl. Catal. A Gen.* **2022**, *638*, 118635.
[51] Bresnehan, M. S.; Hollander, M. J.; Wetherington, M.; LaBella, M.; Trumbull, K. A.; Cavalero, R.; Snyder, D. W.; Robinson, J. A. Integration of hexagonal boron nitride with quasi-freestanding epitaxial graphene: Toward wafer-scale, high-performance devices. *ACS Nano* **2012**, *6*, 5234–5241.
[52] Chalmpes, N.; Bourlinos, A. B.; Alsmaeil, A. W.; Aljarrah, A. S.; Salmas, C. E.; Karakassides, M. A.; Giannelis, E. P. First synthesis of 2D materials by hypergolic reactions and evaluation of their dispersions for ink formulation: Hexagonal boron nitride and fluorinated carbon nanosheets. *Mater. Res. Express* **2024**, *11*, 035002.

[53] Afify, A. S.; Ahmad, S.; Khushnood, R. A.; Jagdale, P.; Tulliani, J. M. Elaboration and characterization of novel humidity sensor based on micro-carbonized bamboo particles. *Sens. Actuators B Chem* **2017**, *239*, 1251–1256.
[54] Duan, Z. H.; Li, J.; Yuan, Z.; Jiang, Y. D.; Tai, H. L. Capacitive humidity sensor based on zirconium phosphate nanoplates film with wide sensing range and high response. *Sens. Actuators B Chem* **2023**, *394*, 134445.
[55] Chen, S. C.; Zhang, T.; Tappertzhofen, S.; Yang, Y. C.; Valov, I. Electrochemical-memristor-based artificial neurons and synapses-fundamentals, applications, and challenges. *Adv. Mater.* **2023**, *35*, 2301924.
[56] Oh, S.; Lee, J. H.; Seo, S.; Choo, H.; Lee, D.; Cho, J. I.; Park, J. H. Electrolyte-gated vertical synapse array based on van der Waals heterostructure for parallel computing. *Adv. Sci.* **2022**, *9*, 2103808.
[57] Gao, F. L.; Min, P.; Ma, Q.; Zhang, T. T.; Yu, Z. Z.; Shang, J.; Li, R. W.; Li, X. F. Multifunctional thermoelectric temperature sensor for noncontact information transfer and tactile sensing in human-machine interaction. *Adv. Funct. Mater.* **2024**, *34*, 2309553.
[58] Wu, B. W.; Jiang, T.; Yu, Z. X.; Zhou, Q. H.; Jiao, J.; Jin, M. L. Proximity sensing electronic skin: Principles, characteristics, and applications. *Adv. Sci.* **2024**, *11*, 2308560.
[59] Qin, J. X.; Shen, C. L.; Li, L.; Liu, H.; Zhang, W. Y.; Yang, X. G.; Shan, C. X. Broadband negative photoconductive response in carbon nanodots. *Adv. Mater.* **2024**, *36*, 2404694.
[60] Zhao, X. L.; Zhou, K. L.; Zhong, Y. J.; Liu, P.; Li, Z. C.; Pan, J. L.; Long, Y.; Huang, M. R.; Brakat, A.; Zhu, H. W. Hydrophobic ionic liquid-in-polymer composites for ultrafast, linear response and highly sensitive humidity sensing. *Nano Res.* **2021**, *14*, 1202–1209.
[61] Zhang, D. Z.; Wang, M. Y.; Tang, M. C.; Song, X. S.; Zhang, X. X.; Kang, Z. J.; Liu, X. H.; Zhang, J. H.; Xue, Q. Z. Recent progress of diversiform humidity sensors based on versatile nanomaterials and their prospective applications. *Nano Res.* **2023**, *16*, 11938–11958.
[62] Hou, Y. B.; Gao, M.; Gao, J. W.; Zhao, L. H.; Teo, E. H. T.; Wang, D.; Qi, H. J.; Zhou, K. 3D printed conformal strain and humidity sensors for human motion prediction and health monitoring via machine learning. *Adv. Sci.* **2023**, *10*, 2304132.
[63] Qin, J. X.; Yang, X. G.; Shen, C. L.; Chang, Y.; Deng, Y.; Zhang, Z. F.; Liu, H.; Lv, C. F.; Li, Y. Z.; Zhang, C. et al. Carbon nanodot-based humidity sensor for self-powered respiratory monitoring. *Nano Energy* **2022**, *101*, 107549.
[64] Kresse, G.; Furthmüller, J. Efficient iterative schemes for *ab initio* total-energy calculations using a plane-wave basis set. *Phys. Rev. B* **1996**, *54*, 11169–11186.
[65] Kresse, G.; Joubert, D. From ultrasoft pseudopotentials to the projector augmented-wave method. *Phys. Rev. B* **1999**, *59*, 1758–1775.
[66] Qi, C. C.; Xu, X. H.; Wang, D. L.; Feng, Y.; Zhang, Q. L.; Chen, Q. S. Coverage-dependent adsorption of H_2O on dicalcium silicate (100) surface: A DFT study. *Constr. Build. Mater.* **2022**, *321*, 126403.
[67] Li, Z. K.; Zhang, S. M.; Chen, Y. H.; Ling, H. N.; Zhao, L. B.; Luo, G. X.; Wang, X. C.; Hartel, M. C.; Liu, H.; Xue, Y. M. et al. Gelatin methacryloyl-based tactile sensors for medical wearables. *Adv. Funct. Mater.* **2020**, *30*, 2003601.
[68] Lu, L. J.; Jiang, C. P.; Hu, G. S.; Liu, J. Q.; Yang, B. Flexible noncontact sensing for human-machine interaction. *Adv. Mater.* **2021**, *33*, 2100218.
[69] Yu, J.; Feng, Y. F.; Sun, D.; Ren, W. F.; Shao, C. Y.; Sun, R. C. Highly conductive and mechanically robust cellulose nanocomposite hydrogels with antifreezing and antidehydration performances for flexible humidity sensors. *ACS Appl. Mater. Interfaces* **2022**, *14*, 10886–10897.